Photoacoustic tomography and fluorescence molecular tomography: A comparative study based on indocyanine green

Bo Wang[a)] and Qing Zhao[a)]
Department of Biomedical Engineering, University of Florida, Gainesville, Florida 32611

Natalie M. Barkey and David L. Morse
Department of Experimental Imaging, Lee Moffitt Cancer Center & Research Institute, Tampa, Florida 33612

Huabei Jiang[b)]
Department of Biomedical Engineering, University of Florida, Gainesville, Florida 32611

Purpose: Both photoacoustic tomography (PAT) and fluorescence molecular tomography (FMT) can be used for molecular imaging when contrast agents are administrated. The goal of this work is to comparatively evaluate the performance of reflection-mode PAT and FMT in common phantom when indocyanine green (ICG) was used as a contrast agent.
Methods: Reflection-mode PAT and FMT systems were developed. Target embedded in a background phantom with different ICG concentration, size, and depth location was examined. Comparisons were made in terms of target morphology, spatial resolution, and sensitivity between the two modalities.
Results: Phantom results showed that PAT and FMT gave different image morphology. PAT offered higher spatial resolution, while FMT provided higher sensitivity. Thus, improved target detection could be achieved by correlating the complementary information obtained from the two modalities.
Conclusions: The combination of high resolution PAT and high sensitivity FMT will provide a more complete range of pathology spectra for more reliable target detection, suggesting a potentially better diagnostic tool when this combination coupled with the administration of ICG as contrast agent is applied to clinical problems in the future. © *2012 American Association of Physicists in Medicine*. [http://dx.doi.org/10.1118/1.3700401]

Key words: photocoustic tomography, fluorescence molecular tomography, reflection mode

I. INTRODUCTION

In recent years, fluorescence molecular tomography (FMT) has received particular attention. This is mainly due to its remarkably increased sensitivity as well as the increasing availability of fluorescent dyes and probes, which provide a variety of molecular signatures. Quantitative three dimensional imaging of fluorescent probes are achievable for phantom experiments[1–3] and animal models.[4–6] In order to apply this technology for clinical applications such as intraoperative imaging, reflection-mode FMT systems were developed by several groups.[3,7–9] However, the major limitation of FMT is its low spatial resolution, especially in reflection-mode.

Photoacoustic tomography (PAT) is an emerging hybrid modality that combines strong endogenous and exogenous optical contrast with high ultrasonic spatial resolution.[10–12] It overcomes the diffusion limit of optical imaging and thus improves the spatial resolution. 3D reflection-mode PAT can be achieved by point-scanning the dual foci of optical illumination and ultrasound detection, or achieved by tomography reconstruction using signal from an unfocused transducer array. The major limitation of PAT is relatively lower sensitivity compared to FMT when near-infrared (NIR) fluorescent dyes such as ICG are used.

Various contrast agents are used to improve the PAT image quality, most of which have fluorescent properties. In this case, a dual imaging modality of PAT and FMT can be realized simultaneously. Together, PAT offers excellent spatial resolution, and FMT provides high sensitivity, making the combination ideal for improvement of possible clinical applications. With the development of NIR fluorophores and nanomaterials over the past several years, considerable image quality enhancement has been achieved for both PAT (Refs. 13, 14) and FMT.[15–17] When the NIR fluorophores are conjugated to a specific targeting ligand, excellent signal to background ratio can be obtained even in deep tissues.

Initial work has been done toward combining PAT and FMT modalities. Razansky demonstrated that the image quality of FMT reconstruction can be improved using *a priori* photoacoustic absorption distribution, in which the target information is only acquired by FMT, hence lacking much improvement in spatial resolution.[18] Others have shown both PAT and two dimensional planar fluorescence imaging results of lymph node and brain structures in small animals.[19–21] However, little effort has been made to compare the two methods using reflection mode fluorescence imaging, nor toward exploring the potential of combining the two methods for *in vivo* applications.

To our knowledge, this is the first time that the performance of reflection-mode three dimensional FMT and PAT are investigated systematically in common phantoms, in which ICG was used as a contrast agent.

II. MATERIALS AND METHODS

II.A. PAT

The three-dimensional photoacoustic system is shown in Fig. 1(a). A tilted fiber bundle delivers laser light from a Ti:sapphire tunable laser providing a generally homogeneous illumination. The incident intensity is up to 20 mJ/cm^2 on the object surface, which is 100% of the American National Standards Institute limit.[22] The laser source has a repetition rate of 10 Hz, and the pulse duration is about 6 ns. Different laser wavelengths were chosen for the different ICG concentrations in the phantom experiments so that the absorption peak of ICG could be reached. A 4 MHz immersion US transducer was scanned in the two transverse directions using a step linear stage, and there were 20 steps for both x and y directions with step sizes of 1.27 and 1 mm, respectively. The generated photoacoustic waves were averaged 50 times for each position; thus, it took about 40 min for a complete volume scan. The complex signal was amplified by a commercial preamplifier and acquired by a high-speed PCI data acquisition board. A LabView program controlled the entire system for data acquisition, following which the volumetric images within the phantom were reconstructed by applying the limited-field-filtered back-projection algorithm.[23]

II.B. FMT

The experimental FMT setup is shown in Fig. 1(b). A continuous wave (CW) 785 nm diode laser (Model DL7140-201 S, Sanyo, Japan) was mounted on a linear stage (Model 17AMA045, CVI Melles Griot) to deliver excitation light through a convex lens to specific points, which had an incident power of 20 mW. A CCD camera (Princeton Instrument, Trenton, NJ) coupled with a 1024 × 1024 pixel array was placed facing the surface of the phantom in reflection mode. The angle between the laser beam and the camera was about 15°. An 830 nm band-pass filter (Thin Film Imaging Technologies, MA) was employed in front of the camera to eliminate the excitation light. For each experiment, the exposure time of the CCD camera was varied, and pixel binning was used for improved signal to noise ratio. In our study, a total of 36 source positions were used and 45 detector

positions were selected from the images acquired by CCD camera covering an area of 20 × 20 mm in the X-Y plane.

The fluorescence images obtained were reconstructed using an iterative finite element based algorithm that was described in detail previously.[24] Here, we describe the FMT reconstruction process in brief. The photon diffuse equation

$$\nabla \cdot [D_m(r)\nabla\varphi_m(r)] - \mu_{a_m}(r)\varphi_m(r) + \eta\mu_{a_{x\rightarrow m}}(r)\varphi_x(r) = 0 \tag{1}$$

coupled with type III boundary conditions, $-D_{x,m}\nabla\varphi_{x,m} \cdot \hat{n} = \alpha\varphi_{x,m}$, is transformed into the following matrix form of:

$$[A_{x,m}]\{\varphi_{x,m}\} = \{b_{x,m}\} \tag{2}$$

by the finite element discretization, where $\varphi_{x,m}$ is the photon density; $D_{x,m} = 1/3\left(\mu_{a_{x,m}}(r) + \mu'_{s_{x,m}}(r)\right)$ is the diffusion coefficient; $\mu_{a_{x,m}}$ and $\mu'_{s_{x,m}}$ represent the absorption coefficient and the reduced scattering coefficient for excitation and emission, respectively; and $\eta\mu_{a_{x-m}}$ is the fluorescence quantum yield. The elements of matrix [A] and the entries in column vectors $b_{x,m}$ can be expressed by a set of spatially varying Lagrangian basis functions.[25,26] A finite element is applied to model the diffusion equation.

III. EXPERIMENTS AND RESULTS

ICG is a FDA approved fluorescent contrast agent that can be used for both fluorescence and photoacoustic imaging. ICG absorbs light primarily in the range of 600 and 900 nm and emits fluorescence light from 750 to 950 nm. It has a molar extinction coefficient of $2 \times 10^4 \sim 1 \times 10^5$ cm^{-1}/M, depending on the excitation wavelength,[27] and a quantum yield of ~0.027,[28] when the concentration is less than 1 mM in water in its absorption spectrum range. To comparatively evaluate the performance of FMT and PAT, the same ICG containing phantoms were used for both modalities and the reconstructed FMT and PAT images were compared in terms of the image pattern/morphology, spatial resolution, and sensitivity. The background phantom was composed of 0.7% Intralipid, India ink, and 2% agar powder providing $\mu_a = 0.01$/mm and $\mu'_s = 0.7$/mm. The targets were different in size, number, and ICG concentration for different experiments. The reconstructed volume was 2 cm × 2 cm × 2 cm for FMT, while for PAT the reconstructed volume was 2 cm × 2 cm × 1.7 cm, which was 3 mm below the surface to avoid the strong surface signal. When comparing the image pattern and spatial resolution, a wavelength of 810 nm and a laser energy density of 3 mJ/cm^2 on the phantom surface were used for PAT. For sensitivity study, different wavelengths at a laser energy density of 20 mJ/cm^2 were used for PAT, while one excitation wavelength at a fixed incident laser power was used for FMT.

III.A. Comparison of image pattern

One cylindrical solid target with a diameter of 2 mm and a height of 1 mm was embedded in the center of a cubic background phantom. ICG concentration of the target was
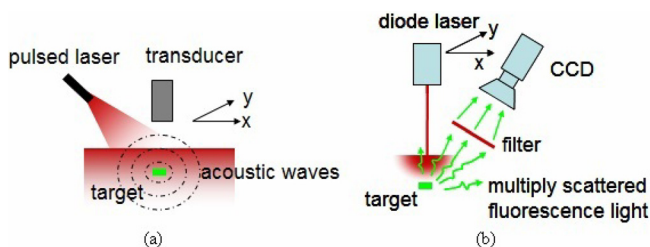

FIG. 1. Schematic of the (a) PAT and (b) FMT systems.

100 μM. Some simulations were also done for validating the PAT result.

Figure 2 represents the reconstructed results of PAT and FMT. Figures 2(a) and 2(b) are the reconstructed PAT images along the Z-X (Y = 10) and X-Y (Z = 7) slices with the exact location of the targets indicated by the white lines for comparison. Figures 2(c) and 2(d) are the corresponding results of FMT. The imaging planes given in Z direction are from −1 mm to 19 mm and from 0 to 20 mm for PAT and FMT, respectively. We note that the target was clearly detected by both methods. However, the two methods show different patterns, which is clearly seen in Figs. 2(a) and 2(c). In Fig. 2(a), the target is clearly verified with high spatial-resolution, and it is noted that strong signal is observed at the top and bottom surfaces of the target and that the other boundaries and inner volume were not reconstructed. In addition, the phantom surface (i.e., Z = 0 mm) is revealed. In contrast, the FMT reconstructed target size is significantly overestimated with the center position shifted by 1 mm. Although the spatial resolution is not high compared to the PAT images, the FMT images show clear target reconstructions.

To explain these artifacts in detail, time domain PAT simulations using the finite element method (FEM) were performed and compared with the phantom results.[29] The simulation geometry is shown in Fig. 3(a) where a 2D square region (3 mm × 3 mm) contains a smaller rectangular target (2 mm × 1 mm), which is 1.5 mm from the top boundary. Two sets of simulations were performed. In the first set, 41 detectors were evenly distributed along the top boundary of the background region; while in the second set 160 detectors were distributed around all four boundaries. After the time-domain forward data were generated, some band pass filters were applied to simulate experimental data in different frequency ranges. Then, the reconstruction was carried out afterwards. Each simulation set had eight cases, and for each case, the
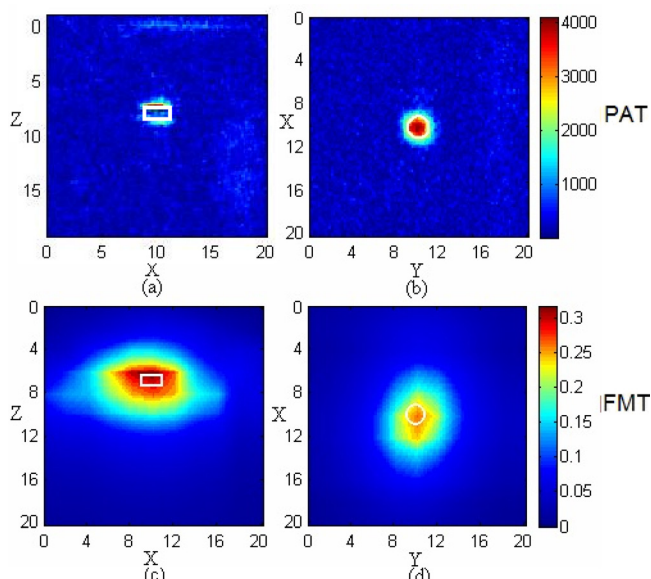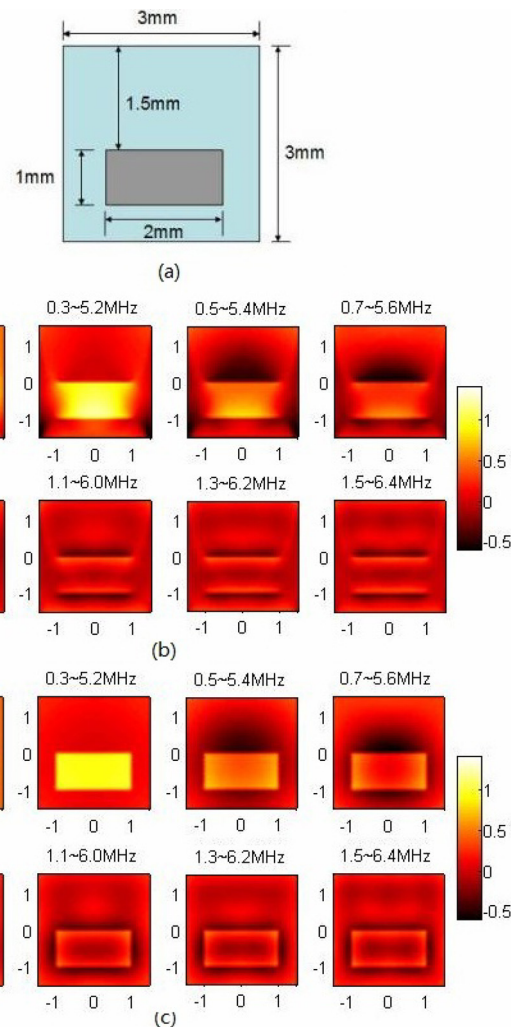

FIG. 3. PAT simulations with time domain finite element method. (a) Simulation geometry; (b) simulation results of different frequency ranges when detectors are placed along the top boundary; (c) simulation results of different frequency ranges when detectors are positioned along all four boundaries. The color scale records the absorption coefficient in mm^{-1}.

frequency band width was 5 MHz with a slightly different initial frequency. The target to background absorption contrast ratio was 3:1. There were 200 time steps, and the time interval was 0.02 μs, and the velocity of the sound was chosen to be 1.495 mm/μs in water. The mesh had 1415 nodes. The two sets of simulation results are shown in Figs. 3(b) and 3(c), respectively.

It can be seen that, as the frequency range changes, the reconstructed image varies in pattern and intensity. In Fig. 3(b), it is noted that when the initial frequency is small, the target is well reconstructed; but when the initial frequency increases to 0.9 MHz, only the top and bottom boundaries are reconstructed, which is very similar to the experimental cases. In contrast, in the second simulation set shown in Fig. 3(c), all four target boundaries are well reconstructed, although as the initial frequency increases the inner area is again not perfectly reconstructed. This implies that detector distribution and lack of low frequency information mainly account for the artifacts in the reflection mode experiments. In fact, when the targets are large or the frequency is higher, we only receive signal
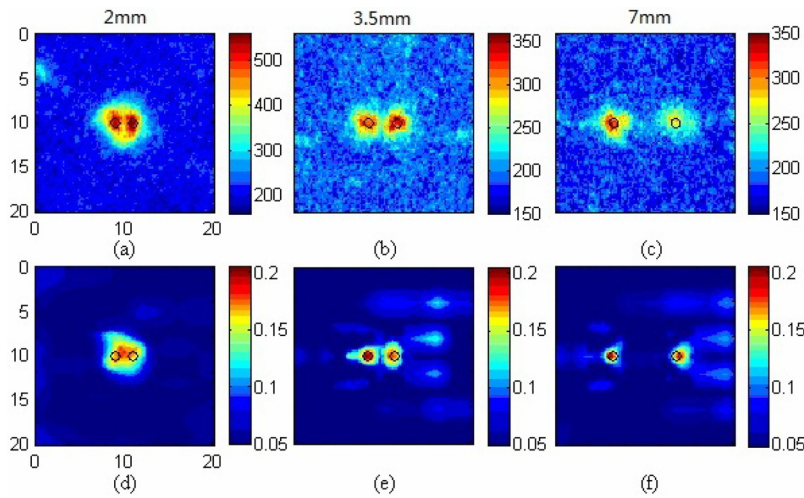

FIG. 2. PAT and FMT images for a 100 μM ICG target at 7 mm depth. (a) and (b) Z-X image, X-Y PAT image; (c) and (d) corresponding FMT image. The white lines indicate the exact target location.

FIG. 4. Reconstructed images with different target separations. (a)–(c) PAT images; (d)–(f) FMT images.

from the boundaries of the targets.[30] For our transducer, the half width of the frequency response is from 2.53 to 5.42 MHz, which is quite high for the target in our experiment compared to the simulation results. Besides, the signal intensity is related to the beam angle, so that only the boundaries of the targets that are nearly perpendicular to the axis of the transducer can be clearly imaged.[31] Therefore, we can only get the top and bottom boundaries reconstructed in our experiments. This kind of result is widely seen in other similar published experiments.[32]

III.B. Comparison of spatial resolution

In this case, there were three sets of phantom experiments. Two cylindrical targets (1 mm diameter and 1 mm height)

were located at a 7 mm depth. The separation between the centers of the two targets differed by 2, 4, and 6 mm, respectively, in the horizontal plane. Each target contained 100 μM ICG.

Figure 4 shows the reconstructed PAT and FMT results of the two targets with different horizontal separations. Figures 4(a)–4(c) are the PAT images, which are the average absorption projections in the x-y plane. Figures 4(d)–4(f) are the X-Y cross section images of FMT at the target position. The exact target positions are indicated by black lines. For both methods, the two targets are clearly reconstructed, and we can see that the targets move further apart as their separation increases. However, it is noted that for FMT, the images of the two targets are not fully separated when they are only 2 mm apart; but they are clearly separated by PAT, which
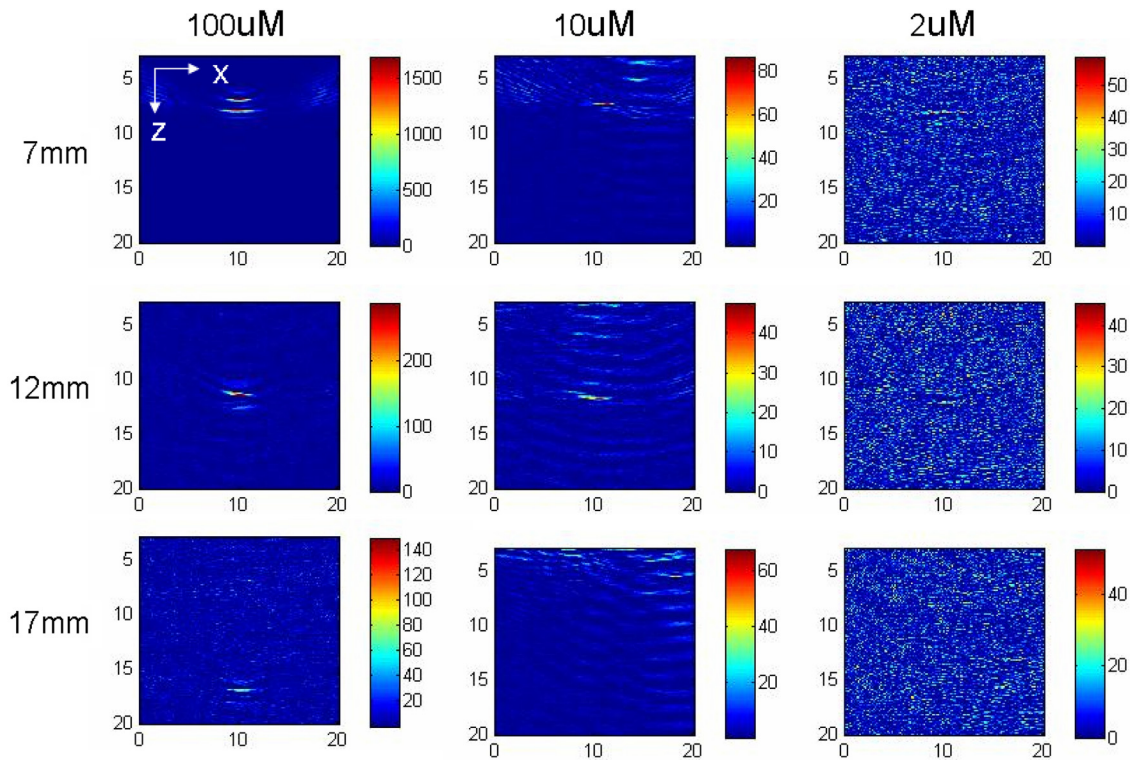

FIG. 5. PAT images for a target with different ICG concentration at different depth.

proves that the spatial resolution of PAT is higher than FMT. This may due to the strong scattering of the fluorescence light in FMT while the ultrasound scattering and attenuation is relatively small in PAT.

III.C. Comparison of sensitivity

A total of nine sets of phantom experiments were conducted, which involved three different ICG concentrations and three different depths. The three different concentrations were 100, 10, and 2 μM. Correspondingly, three different wavelengths (698, 780, and 790 nm) were used for PAT at the three different ICG concentrations. These wavelengths represent the peak absorption at each of the three ICG concentrations.[27] For each concentration, the targets were buried at 7, 12, and 17 mm, respectively. The targets were 2 mm in diameter and 1 mm in height.

Figure 5 shows the reconstructed X-Z (Y = 10) PAT images, while Fig. 6 shows the corresponding FMT results. In Fig. 6, the black rectangles indicate the exact target positions, while the PAT results provide much more reliable target position and size because of the high spatial resolution. In Fig. 5, it can be seen that as the ICG concentration decreases or the target position goes deeper, the reconstructed image has greater artifacts and decreased image quality. While similar trend is seen from the FMT images, we note that FMT has much greater sensitivity compared to PAT for detection of ICG fluorochromes. For example, the target with 10 μM ICG at 17 mm depth or 2 μM ICG at 12 mm depth is detected by FMT (Fig. 6), while the corresponding target is not detected by PAT (Fig. 5). This may be due to the fact that both the target and background generated
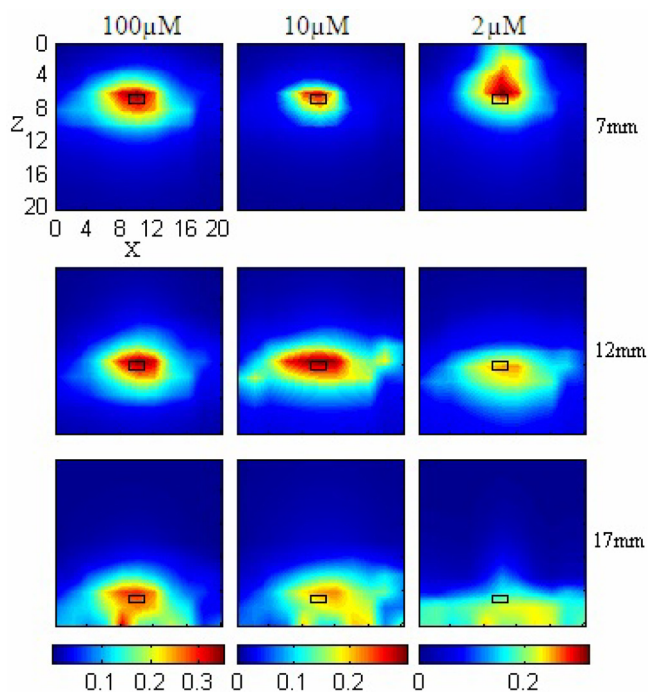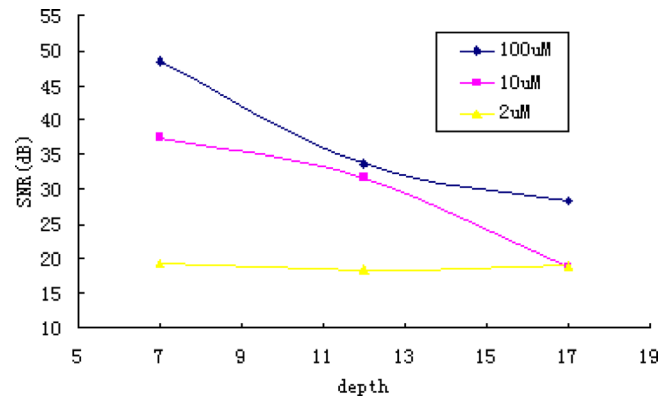

FIG. 7. SNR of PAT images for a target with different ICG concentration at different depth.

ultrasound upon the optical absorption in the case of PAT, while mostly the target produces NIR fluorescent emission and the background almost gives no NIR emission in the case of FMT.

We also calculated the corresponding SNR for PAT, as shown in Fig. 7 where SNR is plotted as a function of the depth for different ICG concentration. In the calculations, the maximal value within the reconstructed target volume of the PAT image was used as the signal, and the averaged value of the background was used as the noise. The measured $1/e$ decay of the signal for 100 and 10 μM were 4.3 and 4.6 cm, respectively, compared to the theoretical value of 6.9 cm. Less penetration depth was obtained, in part, because of the oblique optical fiber position and non optimal area illumination. The SNR for 2 μM at 7 mm depth was about 2.2 dB, giving a measured noise-equivalent sensitivity of 0.22 μM at 7 mm depth.[33]

For FMT, it is noticed from Fig. 6 that the recovered target position has greater errors compared to the cases with smaller target depth or larger fluorochrome concentration. Also, we note some artifacts below the target with 2 μM ICG at the 17 mm depth.

IV. CONCLUSION

We compared PAT and FMT for reflection mode imaging using ICG as the common contrast agent. We have shown that PAT has better spatial resolution and that FMT has better sensitivity. Thus, there is the potential that the two methods combined could improve the reliability of target detection.

However, there are some limitations of our methods. The 3D photoacoustic images were acquired by mechanically scanning the photoacoustic probe, resulting in slow acquisition times. The phantom images were acquired from two separate systems, and the lack of coregistration between the two systems makes the comparison more difficult. Efforts are underway to integrate the PAT and FMT systems in a single platform, so that the PAT and FMT images can be coregistered precisely. In this way, a handheld PAT/FMT probe can be made for clinical use, which we plan to attempt in the future.

FIG. 6. FMT images for a target with different ICG concentration at different depth. The black blocks indicate the true target position.

[a]Bo Wang and Qing Zhao have equal contribution to this work.

[b]Author to whom correspondence should be addressed. Electronic mail: hjiang@bme.ufl.edu

[1]Y. Tan and H. Jiang, "DOT guided fluorescence molecular tomography of arbitrarily shaped objects," Med. Phys. **35**, 5703 (2008).

[2]A. Joshi, W. Bangerth, and E. M. Sevick-Muraca, "Adaptive finite element based tomography for fluorescence optical imaging in tissue," Opt. Express **12**, 5402–5417 (2004).

[3]D. S. Kepshire, S. C. Davis, H. Dehghani, K. D. Paulsen, and B. W. Pogue, "Challenges in sub-surface fluorescence diffuse optical imaging," Proc. SPIE **6434**, 64340R (2007).

[4]Y. Tan, L. Yang, and H. Jiang, "DOT guided fluorescence molecular tomography of tumor cell quantification in mice," in *Biomedical Optics*, OSA Technical Digest (CD) (Optical Society of America, 2010), paper JMA69.

[5]E. Graves, J. Ripoll, R. Weissleder, and V. Ntziachristos, "A submillimeter resolution fluorescence molecular imaging system for small animal imaging," Med. Phys. **30**, 901 (2003).

[6]V. Ntziachristos, E. A. Schellenberger, J, Ripoll, D. Yessayan, E. Graves, A. Bogdanov, L. Josephson, and R. Weissleder, "Visualization of antitumor treatment by means of fluorescence molecular tomography with an annexin V–Cy5.5 conjugate," Proc. Natl. Acad. Sci. U.S.A. **101**, 12294–12299 (2004).

[7]J. Ge, S. Erickson, and A. Godavarty, "Fluorescence tomography imaging using a handheld-probe-based optical imager: extensive phantom studies," Appl. Opt. **48** 6408–6416 (2009).

[8]A. Godavarty, A. B. Thompson, R. Roy, M. J. Eppstein, C. Zhang, M. Gurfinkel, and E. M. Sevick-Muraca, "Diagnostic imaging of breast cancer using fluorescence-enhanced optical tomography: phantom studies," J. Biomed. Opt. **9**, 488–496 (2004).

[9]A. Joshi, W. Bangerth, K. Hwang, J. C. Rasmussen, and E. M. Sevick-Muraca, "Fully adaptive FEM based fluorescence optical tomography from time-dependent measurements with area illumination and detection," Med. Phys. **33**, 1299–1310 (2006).

[10]C. G. A. Hoelen, F. F. M. de Mul, R. Pongers, and A. Dekker, "Three-dimensional photoacoustic imaging of blood vessels in tissue," Opt. Lett. **23**(8), 648–650 (1998).

[11]R. A. Kruger, W. L. Kiser, D. R. Reinecke, G. A. Kruger, and K. D. Miller, "Thermoacoustic molecular imaging of small animals," Mol. Imaging **2**, 113–123 (2003).

[12]X. Wang, Y. Pang, G. Ku, X. Xie, G. Stoica, and L. V. Wang, "Noninvasive laser-induced photoacoustictomography for structural and functional in vivo imaging of the brain," Nat. Biotechnol. **21**, 803–806 (2003).

[13]C. Kim, E. C. Cho, J. Chen, K. H. Song, L. Au, C. Favazza, Q. Zhang, C. M. Cobley, F. Gao, Y. Xia, and L. V. Wang, "*In vivo* molecular photoacoustic tomography of melanomas targeted by bio-conjugated gold nanocages," ACS Nano **4**, 4559–4564 (2010).

[14]John A. Copland, M. Eghtedari, V. L. Popov, N. Kotov, N. Mamedova, M. Motamedi, and A. A. Oraevsky, "Bioconjugated gold nanoparticles as a molecular based contrast agent: Implications for imaging of deep tumors using optoacoustic tomography," Mol. Imaging Biol. **6**, 341–349 (2004).

[15]X. Gao, Y. Cui, R. M. Levenson, L. W. Chung, and S. Nie, "In vivo cancer targeting and imaging with semiconductor quantum dots," Nat. Biotechnol. **22**, 969–976 (2004).

[16]J. H. Lee, Y. M. Huh, Y. W. Jun, J. W. Seo, J. T. Jiang, H. T. Song, S. Kim, E. J. Cho, H. G. Yoon, J. S. Suh, and J. Cheon, "Artificially engineered magnetic nanoparticles for ultra-sensitive molecular imaging," Nat. Med. **13**, 95–99 (2007).

[17]L. Yang, H. Mao, Z. Cao, Y. A. Wang, X. Peng, X. Wang, H. K. Sajja, L. Wang, H. Duan, C. Ni, C. A. Staley, W. C. Wood, X. Gao, S. Nie, "Molecular imaging of pancreatic cancer in an animal model using targeted multifunctional nanoparticles," Gastroenterology **136**, 1514–1525 (2009).

[18]D. Razansky and V. Ntziachristos, "Hybrid photoacoustic fluorescence molecular tomography using finite-element-based inversion," Med. Phys. **34**, 4293 (2007).

[19]C. Kim, K. H. Song, F. Gao, and L. V. Wang, "Sentinel lymph nodes and lymphatic vessels: noninvasive dual-modality in vivo mapping by using indocyanine green in rats—volumetric spectroscopic photoacoustic imaging and planar," Radiology **255**, 442–450 (2010).

[20]X. Xie, J. T. Oh, M. L. Li, G. Ku, X. Wang, S, Ke, C. Li, S. Similache, G. Stoica, and L. V. Wang, "Photoacoustic tomography and molecular fluorescence imaging: dual modality imaging of small animal brains in vivo," Proc. SPIE **5697**, 107–110 (2005).

[21]C. Kim, T. N. Erpelding, L. Jankovic, M. D. Pashley, and L. V. Wang, "Deeply penetrating in vivo photoacoustic imaging using a clinical ultrasound array system," Biomed. Opt. Express **1**(1), 278–284 (2010).

[22]American National Standards Institute, "American national standard for the safe use of lasers," ANSI Z136.1-2000 (American National Standards Institute, New York, NY, 2007).

[23]D. Yang, D. Xing, H. Gu, Y. Tan, and L. Zeng, "Fast multielement phase-controlled photoacoustic imaging based on limited-field-filtered back-projection algorithm," Appl. Phys. Lett. **87**, 194101 (2005).

[24]C. Wu, H. Barnhill, X. Liang, Q. Wang, and H. Jiang, "A new probe using hybrid virus-dye nanoparticles for near-infrared fluorescence tomography," Opt. Commun. **255**, 366–374 (2005).

[25]H. Jiang, "Frequency-domain fluorescent diffusion tomography: A finite element-based algorithm and simulations," Appl. Opt. **37**, 5337–5342 (1998).

[26]Y. Tan and H. Jiang, "Diffuse optical tomography guided quantitative fluorescence molecular tomography," Appl. Opt. **47**, 2011–2016 (2008).

[27]M. L. J. Landsman, G. Kwant, G. A. Mook, and W. G. Zijlstra, "Light-absorbing properties, stability, and spectral stabilization of indocyanine green," J. Appl. Physiol. **40**, 575–583 (1976).

[28]R. Philip, A. Penzkofer, W. Baumler, R. M. Szeimies, and C. Abels, "Absorption and fluorescence spectroscopic investigation of indocyanine," J. Photochem. Photobiol., A **96**, 137–148 (1996).

[29]L. Yao and H. Jiang, "Finite-element-based photoacoustic tomography in time domain," J. Opt. A: Pure Appl. Opt. **11**, 085301 (2009).

[30]S. Park, S. Mallidi, A. B. Karpiouk, S. Aglyamov, and S. Y. Emelianov, "Photoacoustic imaging using array transducer," Proc. SPIE **6437**, 643714 (2007).

[31]D. Yang, D. Xing, S. Yang, and L. Xiang, "Fast full-view photoacoustic imaging by combined scanning with a linear transducer array," Opt. Express **15**(23), 15566–15575 (2007).

[32]A. Q. Bauer, R. E. Nothdurft, L. V. Wang, and J. P. Culver, "Quantitative, high-resolution photoacoustic spectroscopy by combining photoacoustic imaging with diffuse optical tomography," Proc. SPIE **7899**, 78993O (2011).

[33]C. Kim, T. N. Erpelding, L. Jankovic, and L. V. Wang, "Performance benchmarks of an array-based hand-held photoacoustic probe adapted from a clinical ultrasound system for non-invasive sentinel lymph node imaging," Philos. Trans. R. Soc. London **369**, 4644–4650 (2011).